A dynamic stability design strategy for lithium metal solid state batteries

https://doi.org/10.1038/s41586-021-03486-3

Received: 6 November 2020

Accepted: 23 March 2021

Published online: 12 May 2021

Check for updates

Luhan Ye[1] & Xin Li[1]✉

A solid-state electrolyte is expected to suppress lithium (Li) dendrite penetration with high mechanical strength[1–4]. However, in practice it still remains challenging to realise a lithium metal anode for batteries, because micrometre- or submicrometre-sized cracks in ceramic pellets can frequently be generated during battery assembly or long-time cycling[3,5]. Once cracks form, lithium dendrite penetration is inevitable[6,7]. Here we describe a solid-state battery design with a hierarchy of interface stabilities (to lithium metal responses), to achieve an ultrahigh current density with no lithium dendrite penetration. Our multilayer design has the structure of a less-stable electrolyte sandwiched between more-stable solid electrolytes, which prevents any lithium dendrite growth through well localized decompositions in the less stable electrolyte layer. A mechanism analogous to the expansion screw effect is proposed, whereby any cracks are filled by dynamically generated decompositions that are also well constrained, probably by the 'anchoring' effect the decompositions induce. The cycling performance of the lithium metal anode paired with a $LiNi_{0.8}Mn_{0.1}Co_{0.1}O_2$ cathode is very stable, with an 82 per cent capacity retention after 10,000 cycles at a 20C rate (8.6 milliamps per centimetre squared) and 81.3 per cent capacity retention after 2,000 cycles at a 1.5C rate (0.64 milliamps per centimetre squared). Our design also enables a specific power of 110.6 kilowatts per kilogram and specific energy up to 631.1 watt hours per kilogram at the micrometre-sized cathode material level.

Lithium metal is considered the holy grail of the anode for Li-ion batteries owing to its high capacity and energy density[1,2], while single crystal $LiNi_{0.8}Mn_{0.1}Co_{0.1}O_2$ (NMC811) is regarded as the next-generation cathode material[8–10]. Stable cycling of batteries with an NMC811 cathode paired with a lithium metal anode is of a great importance to mobile devices, especially to electrical vehicles. However, the stability of such batteries with most electrolytes, either liquid or solid, is poor. It is known that $Li_{10\pm x}M_{1\pm y}P_{2\pm p}S_{12\pm q}$ (M = Ge, Si) is not stable with lithium metal[11]. Protection layers such as graphite[3] or indium metal[12] are usually applied to insulate the contact between solid electrolytes and the lithium metal. Without such protection, a symmetric battery using pure lithium metal as electrodes and $Li_{10}Ge_1P_2S_{12}$ (LGPS) as electrolyte can fail quickly with a voltage spark (Fig. 1a). Although most sulfide solid electrolytes undergo a certain level of decomposition in contact with Li metal, the Li-argyrodites $Li_{6-y}PS_{5-y}Cl_{1+y}$ are more stable with lithium metal than LGPS[5,13–16]. $Li_{5.5}PS_{4.5}Cl_{1.5}$ (LPSCl) in such a symmetrical battery can thus run for over 150 h (Fig. 1b). However, a short circuit still appears afterwards. Figure 1a, b actually represents two typical failure phenomena, that is, the overpotential ramping up by electrolyte decomposition and the sudden decrease in voltage by short circuit[5,17]. Other than the stability difference with Li metal, the two electrolytes have very similar physical and (electro)chemical properties[12,13,17,18], including ionic and electronic conductivities, particle sizes and mechanical modulus shown in Extended Data Fig. 1 and Extended Data Table 1.

When discharging lithium onto LGPS or LPSCl in asymmetric batteries (Extended Data Fig. 2 and 3), we observed that the surface of LGPS becomes black (Extended Data Fig. 2b), while that of LPSCl shows no notable colour change (Extended Data Fig. 2a, c). X-ray photoelectron spectroscopy (XPS) shows a heavy decomposition of LGPS to reduced S and reduced $Ge^{\sigma+}$, and so on, while LPSCl shows almost no decomposition peaks (Extended Data Fig. 3), suggesting that the shorting of the LPSCl symmetric battery (Fig. 1b) is caused by the Li dendrite penetration. We further designed a symmetric battery about Li metal anodes with the multilayer sequence in the battery as follows: graphite, then LPSCl, then LGPS, then LPSCl, then graphite, and the total thickness of the three electrolyte layers is the same throughout this Article unless otherwise specified. The two LPSCl outer layers are in direct contact with the graphite-protected lithium metal to further protect the interface (electro)chemically. The layer of LGPS added to the system greatly improves the cycling performance of the symmetric battery, indicating that such an electrochemically less stable solid electrolyte with Li metal can, counterintuitively, block the lithium dendrite penetration. The design shows a superior cycling performance for 1,800 h at 0.25 mA cm^{-2} (Fig. 1c), which is substantially better than any batteries with a single type of electrolyte in our tests. A similar performance contrast can be obtained by replacing LGPS with $Li_{9.54}Si_{1.74}(P_{0.9}Sb_{0.1})_{1.44}S_{11.7}Cl_{0.3}$ (LSPS) as the central electrolyte layer (Extended Data Fig. 4).

Furthermore, we demonstrate that the multilayer symmetric battery can cycle at the extremely high current density of 20 mA cm^{-2} with a low overpotential of ~0.5 V without notable signs of short-circuiting at 55 °C (Fig. 1d). The elevated temperature is mainly for a higher ionic conductivity, following the convention for the high-rate test in this

[1]John A. Paulson School of Engineering and Applied Sciences, Harvard University, Cambridge, MA, USA. ✉e-mail: lixin@seas.harvard.edu

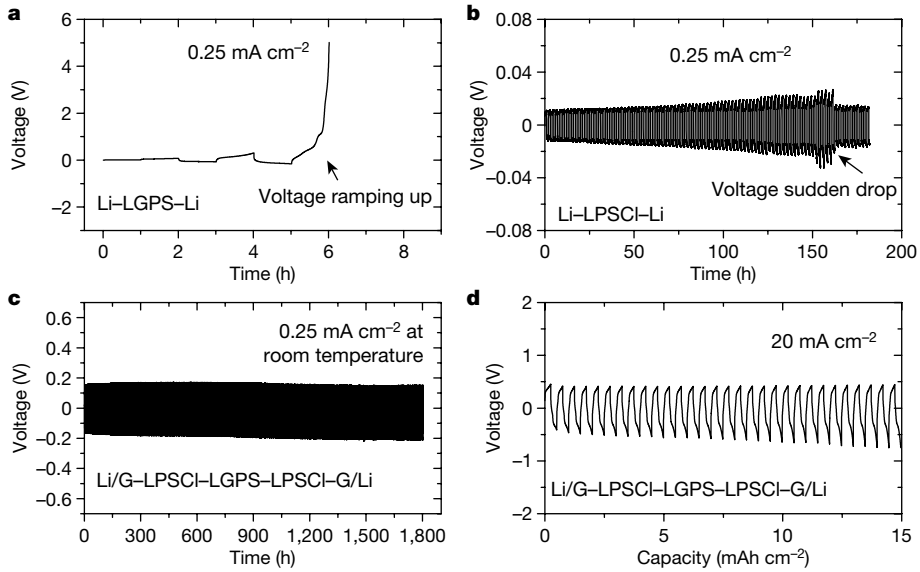

Fig. 1 | Superior symmetric battery cycling performance from the multilayer design. a, **b**, Symmetric battery with $Li_{10}Ge_1P_2S_{12}$ (LGPS) and $Li_{5.5}PS_{4.5}Cl_{1.5}$ (LPSCl) as electrolytes, respectively, and the lithium metal as electrodes, cycling at 0.25 mA cm^{-2} at room temperature for 1 h in each half-cycle. **c**, **d**, Long cycling test (0.25 mA cm^{-2} at room temperature) and high-rate test (20 mA cm^{-2}, at 55 °C), respectively, for the symmetric battery in the configuration of LPSCl–LGPS–LPSCl as electrolyte and graphite-covered lithium (Li/G) as the electrodes, with a capacity of 0.25 mAh cm^{-2} in each half cycle.

field[4,14,19]. This indicates that the structure has good stability to prevent the lithium dendrite penetration. Although the Li/graphite–LGPS–graphite/Li symmetric battery can be tested up to 10 mA cm^{-2}, the overpotential of 1.5 V is much higher, and it cannot last for long cycles or run at higher current density, as shown in Extended Data Fig. 5. Here the LPSCl layer helps stabilize the primary interface to the Li/graphite layer and lower the overall overpotential, making practical cycling at high current density possible.

On the other hand, as shown in Fig. 2a, a black region can be identified in the cross-sectional optical image of the electrolyte pellet after the symmetric battery has run for 300 h at 0.25 mA cm^{-2}. A similar pattern (with more black regions) is observed for the battery after 30 cycles at

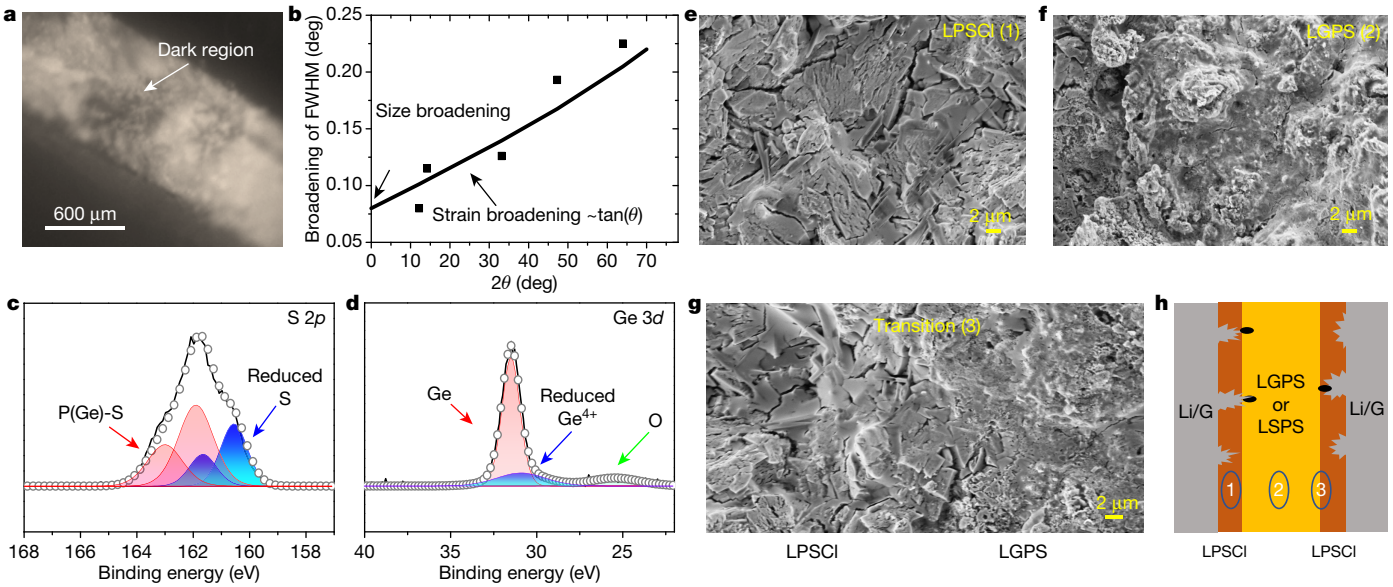

Fig. 2 | Structure, chemistry and morphology of solid electrolyte after cycling. a, Optical image of cross-section of Li/G–LPSCl–LGPS–LPSCl–G/Li after 300 h cycling at 0.25 mA cm^{-2} at room temperature. **b**, XRD peak broadening (increase of full-width at half-maximum (FWHM)) analysis for LGPS after symmetric battery cycling test. Dots are the broadening of different Bragg peaks after 300 h cycling at 0.25 mA cm^{-2}, while the angle dependence for the strain broadening is represented by the solid line, where the *y* intercept represents the level of size broadening. The XRD sample was obtained by cutting through the multilayer pellet and expose the LGPS layer to the surface. **c**, **d**, XPS measurement of S 2*p* (**c**) and Ge 3*d* (**d**) peaks on the black region in the cross-section (similar to **a**) after 30 cycles at 20 mA cm^{-2} at 55 °C. **e**–**h**, SEM images of different cross-section regions of the multilayer on LPSCl (**e**), LGPS (**f**) and LPSCl–LGPS (**g**) transition areas. The images were taken from regions (1), (2) and (3) as illustrated in **h**. The colours in the illustration in **h** represent: silver for Li/Graphite composite layer, where a graphite layer was initially between lithium metal and LPSCl layers but merged quickly with Li metal as one composite layer upon cycling[3]; dark orange for LPSCl layer; light orange for LGPS or LSPS layer; black dots for decomposed LGPS or LSPS with Li dendrite.

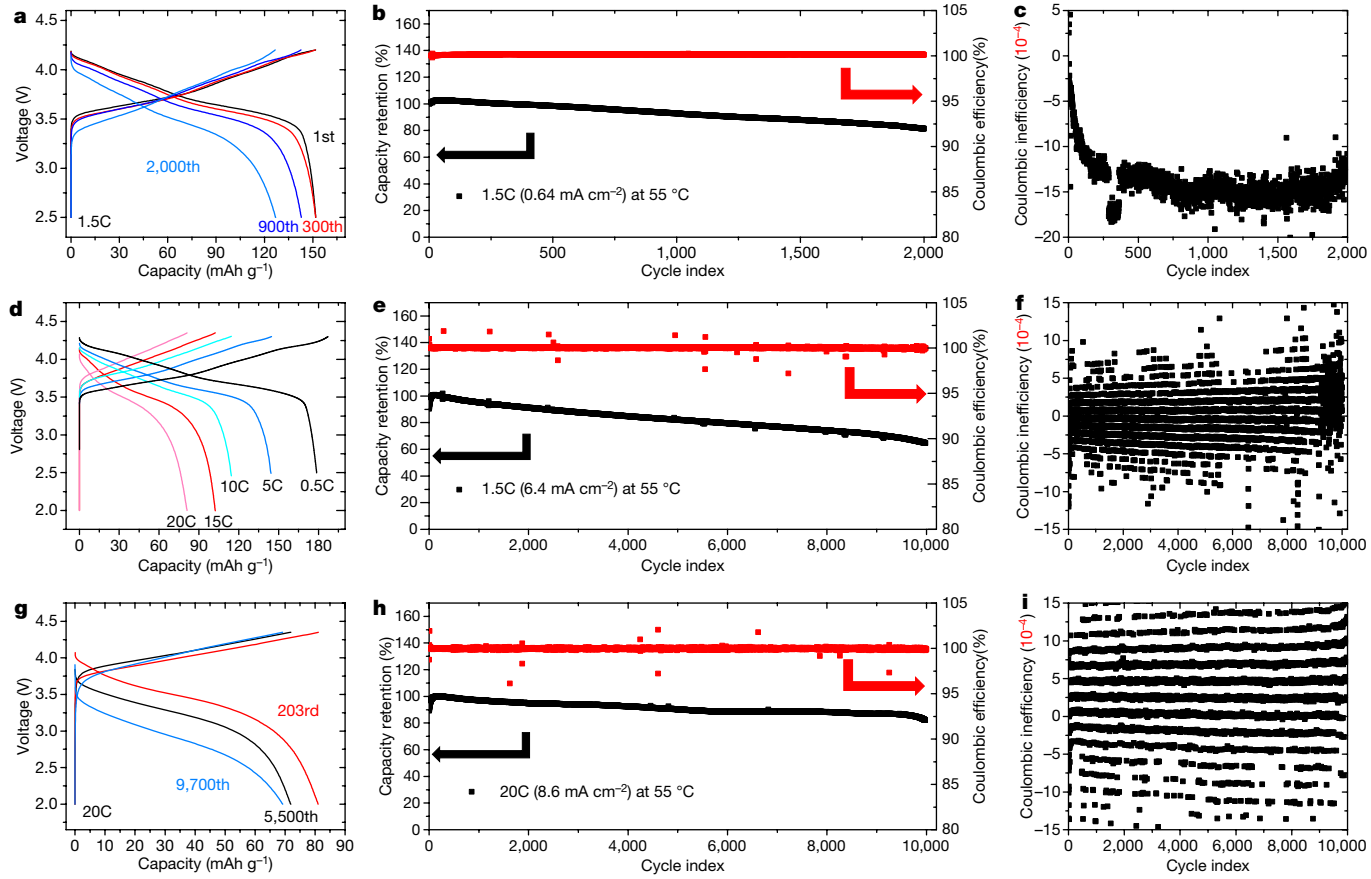

Fig. 3 | Cycling performance of solid-state batteries with the multilayer design. a–c, The charge and discharge profiles (**a**), capacity retention (**b**) and Coulombic inefficiency (**c**) of the battery cycled at 1.5C with cutoff voltages set at 4.2 V and 2.5 V at 55 °C. The anode is Li covered by graphite (Li/G), the cathode is $LiNi_{0.8}Mn_{0.1}Co_{0.1}O_2$ (NMC811), with $Li_{5.5}PS_{4.5}Cl_{1.5}$ (LPSCl) and $Li_{9.54}Si_{1.74}(P_{0.9}Sb_{0.1})_{1.44}S_{11.7}Cl_{0.3}$ (LSPS) as the electrolytes following the multilayer design of LPSCl-LSPS-LPSCl. **d**, Different high-rate initial cycle voltage profiles of batteries charged and discharged at the same rate at 55 °C. The battery shows a discharge capacity of 178.6 mAh g^{-1} at 0.5C, 144.1 mAh g^{-1} at 5C, 114.4 mAh g^{-1} at 10C, 102.2 mAh g^{-1} at 15C, and 81.0 mAh g^{-1} at 20C (8.6 mA cm^{-2}). **e**, **f**, The capacity retention (**e**) and Coulombic inefficiency (**f**) of the battery cycled at 15C with cutoff voltages set at 4.35 V and 2 V at 55 °C. **g–i**, Charge and discharge profiles (**g**), capacity retention (**h**) and Coulombic inefficiency (**i**) of the battery cycled over 10,000 cycles at a rate of 20C with the voltage range 2.0–4.35 V at 55 °C. Here 1C = 0.43 mA cm^{-2}. All batteries in this figure used LPSCl–LSPS–LPSCl as the electrolyte and were tested in an oven with humidity controlled below 10%.

20 mA cm^{-2} (Extended Data Fig. 6a–c). This is the same colour under an optical microscope as the decomposition induced by lithium discharged onto the entire LGPS pellet surface. The black region in the cross-sectional view, however, is only observed in limited regions. The LGPS region was peeled off from the cycled pellet and X-ray diffraction (XRD) was conducted on the surface. Obvious strain broadening of LGPS XRD peaks is observed after symmetrical battery cycling (Fig. 2b and Extended Data Fig. 6f, g). XPS further identifies that the decomposition includes moderately reduced Ge, without the highly reduced Ge state in the Li–Ge alloy, at either a slow rate (Extended Data Fig. 6h–j) or a high rate (Fig. 2c, d). In Fig. 2e–h, scanning electron microscopy (SEM) images were shown for three regions of the multilayer cross-section, that is, LPSCl and LGPS layers and their transition region, from the same symmetric battery after cycling for 300 h. LPSCl shows clear cracks after cycling (Fig. 2e), evolved from the one without observable cracks before cycling (Extended Data Fig. 7). In contrast, the LGPS layer shows no cracks even after cycling (Fig. 2f). Furthermore, compared with the LGPS before cycling, many morphology details are smeared out after cycling, as if it is masked by a 'concrete' layer, suggesting that some local decompositions happened during the cycling.

Under the testing condition of sufficient local mechanical constriction in our all-solid-state battery design, the suppression of Ge reduction here was predicted in computations and observed in XPS[3]. It has also been found that such mechanical constriction can provide metastability around the voltage range of 1–3.5 V[18,20,21]. To further stabilize LGPS towards higher voltages up to 10 V[20], kinetic stability related to ionic passivation was proposed. Specifically, similar strain broadening to Fig. 2b was observed in LGPS charged to and held at 10 V. The strain effect was shown to originate from the local plastic strain field in undecomposed LGPS immediately surrounding the local decomposition front, as the decomposition of sulfide electrolytes often occurs with a positive reaction strain[3,18,20,21].

Here the Li dendrite penetration could also be constricted through such metastability and kinetic stability at the decomposition front, where Ge reduction is suppressed by the local mechanical constriction and the strain field. This well constrained decomposition may serve as a self-healing 'concrete' to fill and heal any micrometre- or submicrometre-sized cracks, either pre-existing during the battery assembly or having emerged during the battery cycling, to inhibit the Li dendrite penetration. In our picture this is analogous to the expansion screw effect, where the Li dendrite is the screw, the decomposition front associated with local strain plays the part of the anchor, and the surrounding pristine electrolyte is the drywall. The central LGPS layer in the multilayer design is thus likely to exhibit such an expansion screw effect, where a self-limiting decomposition at the interface between Li dendrite and solid electrolyte may play a critical part.

We next pair a lithium metal anode with a high-voltage NMC811 cathode of micrometre-sized single-crystal particles. The solid-state battery

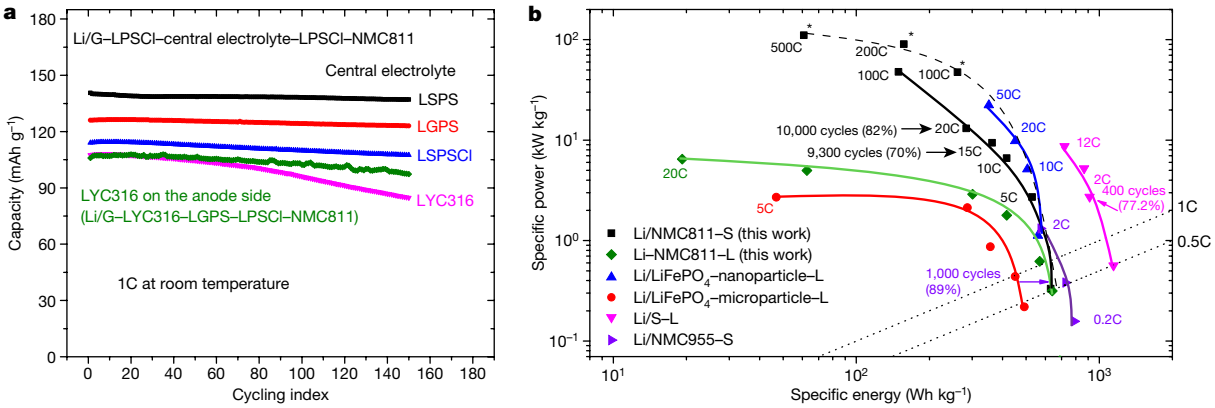

Fig. 4 | Versatility, specific power and energy of the multilayer design. **a**, Battery cycling performance of Li/G-LPSCl-central electrolyte-LPSCl-NMC811 at 1C with cutoff voltages set at 4.3 V and 2 V at room temperature. Various central electrolytes include $Li_{9.54}Si_{1.74}(P_{0.9}Sb_{0.1})_{1.44}S_{11.7}Cl_{0.3}$ (LSPS), $Li_{10}Ge_1P_2S_{12}$ (LGPS), $Li_{9.54}Si_{1.74}P_{1.44}S_{11.7}Cl_{0.3}$ (LSPSCl) and Li_3YCl_6 (LYC316). The green curve represents the battery with the structure of Li/G–LYC316–LGPS–LPSCl–NMC811, where LYC316 serves as a lithium anode stabilizer. **b**, The Ragone plot of the batteries in this study compared with typical performance reported in the field, all with Li metal or equivalent (for example, anode-free) as the anode[14,22–24]. The reported cycling numbers and the capacity retention are labelled for selected data points in the plot, the specific energy and power in the figure are calculated from the mass of the cathode active material. S and L represent solid and liquid electrolyte batteries, respectively. NMC955 represents $LiNi_{0.90}Co_{0.05}Mn_{0.05}O_2$. Lines are drawn to guide the eye. *These batteries were charged slowly at 0.5C and discharged at 100C, 200C and 500C, connected by the dashed grey line. All other data connected by solid lines are from the same charge and discharge rate, with our high-power charge and discharge curves shown in Extended Data Fig. 8m.

with our multilayer design shows substantially improved battery performances, as shown in Fig. 3, compared with the conventional ones in Extended Data Fig. 8. To mimic the more perfect sealing of an industrial pouch cell, we perform most cycling tests in an environmental chamber with humidity control. At elevated temperature (55 °C) and low cycling rate of 1.5C, the solid-state battery shows a 155.7 mAh g^{-1} initial capacity, an outstanding capacity retention of 92.8% at the 1,000th cycle and 81.3% at the 2,000th cycle (Fig. 3a–c). Furthermore, the solid-state battery after 1,000 cycles at 5C can be cycled back to 153.0 mAh g^{-1} at 0.1C after the 5C long cycling test (Extended Data Fig. 8b). This means that after application in electrical vehicles, such batteries can be re-used in a stationary energy storage system. Additional battery cycling testing at 10C can be found in Extended Data Fig. 8c.

To further demonstrate the dendrite suppression ability of our multilayer design, we cycle the battery at 15C (6.4 mA cm^{-2}) and 20C-rate (8.6 mA cm^{-2}) up to 10,000 cycles. The battery shows a capacity retention of 90% after 2,500 cycles, 80% after 5,700 cycles and 70% after 9,300 cycles at 15C (Fig. 3e) and a Coulombic inefficiency on the order of 10^{-4}–10^{-5} (Fig. 3f). At the high C-rate of 20C, the charge and discharge profiles (Fig. 3g) still show very limited shape changes after long cycling, and the capacity retention is as high as 90% after 5,000 cycles and 82% after 10,000 cycles (Fig. 3h) with Coulombic inefficiency on the order of 10^{-3}–10^{-4} (Fig. 3i). The high Columbic efficiency together with long cycling life at such a high current density indicates that no detrimental side reactions and dendrite penetrations happened in the system, which has not been reported for lithium metal battery systems, whether the electrolyte is solid or liquid, making this design competitive with commercial Li-ion batteries having a graphite anode. We note that repetitive cycling at such a high current density is one of the most effective ways to promote dendrite growth, which will quickly short-circuit most previous battery designs with a Li metal anode, whether it is alloyed or protected by a buffer layer or not. We note that the small negative sign in the efficiency here indicates that a small amount of lithium was replenished from the lithium metal anode. This is the advantage of a lithium metal anode over an anode-free battery[14], as even a very thin layer of lithium metal can be beneficial to the cycling performance.

For comparison, batteries with a single type of solid electrolyte are tested in Extended Data Fig. 8d–i. The Li–LPSCl–LCO or Li/G–LPSCl–NMC811 batteries can cycle for a while initially, but all end up with fast capacity fading due to short-circuiting, while such batteries using LGPS fail at the initial cycle. These results are consistent with the symmetric battery tests discussed in Fig. 1. The constructions of all the batteries are summarized in Extended Data Table 2. Furthermore, the Li/G capacity ratio in the anode composite can be further increased to 10:1, equivalent to an anode specific capacity of around 2,000 mAh g^{-1}, indicating plenty of scope to further engineer the battery energy density (Extended Data Fig. 8j). Meanwhile, we have demonstrated that the operating stack pressure can be easily reduced to 50–75 MPa without sacrificing the electrochemical performance of our design (Extended Data Fig. 8k).

We emphasize that this multilayer design is not limited to any specific materials. We demonstrate the versatility of such a design in Fig. 4a: stable cycling is observed with various electrolytes as the central layer (probably attributable to the expansion screw effect that limits Li dendrite penetration), which could be LGPS, LSPSCl and LSPS. However, Li_3YCl_6, which is known to be more stable with Li metal[25], shows an clear capacity decay as the central layer, probably due to the insufficient expansion screw effect. Following this design principle, broad types of solid electrolyte can be included, such as polymers, gels, or sulfides, halides, oxides, phosphates and nitrates, as long as they are in the correct place in the multilayer design according to their (in)stabilities. Furthermore, other cathode materials like sulfur (or selenium) that exhibit promising high capacity and energy density could also be compatible with our multilayer design.

By implementing these solid electrolytes that simultaneously exhibit other good properties, such as high ionic conductivity and air stability, the specific power and energy of the battery can be further optimized. The Ragone plot in Fig. 4b shows that the cyclability, stability, specific energy and power in this solid multilayer design are all orders of magnitude higher than other Li metal anode batteries using micrometre-sized cathode particles, whether with a liquid or solid electrolyte battery[14,22–24]. Specifically, our design actually makes the NMC811 (grey solid and dashed curves) show substantially different behaviour in the Ragone plot from the liquid electrolyte control batteries (green curve), enabling the micrometre-sized single crystal cathode particles to show an attractive high-power performance as the nanometre-sized $LiFePO_4$ in liquid electrolyte batteries (blue triangles)[24].

Another very promising aspect of our design is that the stability of the multilayer structure originates from the designed combination

of (electro)chemical stability and instability, which is not sensitive to the thickness and the micrometre-sized crack density of the electrolyte layers in the initial battery assembly, so that the electrolyte layer thickness can be further reduced (Extended Data Fig. 8l). This strategy of designing instability for dynamic stabilization is different from the conventional wisdom in the field of designing the stability to mechanically block the Li dendrite penetration, which naturally requires a thick and crack-free electrolyte layer. From an engineering perspective, we expect that the flexibility and versatility inherent in our multilayer design will make it compatible with mass-production procedures in the battery industry, where the thickness and mechanical flexibility of the electrolyte layer can be further optimized in the future without sacrificing the safety and performance demonstrated in this Article.

It is worth noting that many factors can influence Li metal (in) stability and the Li dendrite suppression ability of solid electrolytes, which are two related but different concepts, as we have demonstrated in this paper. These factors include mechano-chemical effects[5,7,26], the constriction-modulated decompositions at 0 V (ref. [3]), the constriction-induced metastability and kinetic stability as initially emphasized in the cathode voltage range[20] and generalized here to the proposed expansion screw effect with Li metal, as well as partially reversible decompositions[16,27]. A further exploration of these effects will improve the electrolyte material design by enabling controllable electrochemical (in)stability for both cathode and anode applications. Furthermore, for solid-state battery testing in the field, a further reduction of the stack pressure to a few megapascals or even lower is important to a practical industrial application, which we believe is feasible through material and device designs by further implementing the spirit of the proposed effects here, as well as other ceramic engineering approaches[7,14].

Online content

Any methods, additional references, Nature Research reporting summaries, source data, extended data, supplementary information, acknowledgements, peer review information; details of author contributions and competing interests; and statements of data and code availability are available at https://doi.org/10.1038/s41586-021-03486-3.

1. Goodenough, J. B. & Park, K. S. The Li-ion rechargeable battery: a perspective. *J. Am. Chem. Soc.* **135**, 1167–1176 (2013).
2. Liu, J. et al. Pathways for practical high-energy long-cycling lithium metal batteries. *Nat. Energy* **4**, 180–186 (2019).
3. Su, Y. et al. A more stable lithium anode by mechanical constriction for solid state batteries. *Energy Environ. Sci.* **13**, 908–916 (2020).
4. Chen, Y. et al. Li metal deposition and stripping in a solid-state battery via Coble creep. *Nature* **578**, 251–255 (2020).
5. Kasemchainan, J. et al. Critical stripping current leads to dendrite formation on plating in lithium anode solid electrolyte cells. *Nat. Mater.* **18**, 1105–1111 (2019).
6. Tu, Q., Barroso-Luque, L., Shi, T. & Ceder, G. Electrodeposition and mechanical stability at lithium-solid electrolyte interface during plating in solid-state batteries. *Cell Rep. Phys. Sci.* **1**, 100106 (2020).
7. Qi, Y., Ban, C. & Harris, S. J. A new general paradigm for understanding and preventing Li metal penetration through solid electrolytes. *Joule* **4**, 2599–2608 (2020).
8. Xu, C. et al. Bulk fatigue induced by surface reconstruction in layered Ni-rich cathodes for Li-ion batteries. *Nat. Mater.* **20**, 84–92 (2021).
9. Xin, F. et al. Li-Nb-O coating/substitution enhances the electrochemical performance of the $LiNi_{0.8}Mn_{0.1}Co_{0.1}O_2$ (NMC 811) cathode. *ACS Appl. Mater. Interfaces* **11**, 34889–34894 (2019).
10. Sallard, S., Billaud, J., Sheptyakov, D., Novák, P. & Villevieille, C. Cr-doped Li-rich nickel cobalt manganese oxide as a positive electrode material in Li-ion batteries to enhance cycling stability. *ACS Appl. Energy Mater.* **3**, 8646–8657 (2020).
11. Wenzel, S. et al. Direct observation of the interfacial instability of the fast ionic conductor $Li_{10}GeP_2S_{12}$ at the lithium metal anode. *Chem. Mater.* **28**, 2400–2407 (2016).
12. Kamaya, N. et al. A lithium superionic conductor. *Nat. Mater.* **10**, 682–686 (2011).
13. Adeli, P. et al. Boosting solid-state diffusivity and conductivity in lithium superionic argyrodites by halide substitution. *Angew. Chem. Int. Ed.* **58**, 8681–8686 (2019).
14. Lee, Y. G. et al. High-energy long-cycling all-solid-state lithium metal batteries enabled by silver–carbon composite anodes. *Nat. Energy* **5**, 299–308 (2020).
15. Wenzel, S., Sedlmaier, S. J., Dietrich, C., Zeier, W. G. & Janek, J. Interfacial reactivity and interphase growth of argyrodite solid electrolytes at lithium metal electrodes. *Solid State Ion.* **318**, 102–112 (2018).
16. Auvergniot, J. et al. Interface stability of argyrodite Li_6PS_5Cl toward $LiCoO_2$, $LiNi_{1/3}Co_{1/3}Mn_{1/3}O_2$, and $LiMn_2O_4$ in bulk all-solid-state batteries. *Chem. Mater.* **29**, 3883–3890 (2017).
17. Krauskopf, T., Richter, F. H., Zeier, W. G. & Janek, J. Physicochemical concepts of the lithium metal anode in solid-state batteries. *Chem. Rev.* **120**, 7745–7794 (2020).
18. Wu, F., Fitzhugh, W., Ye, L., Ning, J. & Li, X. Advanced sulfide solid electrolyte by core-shell structural design. *Nat. Commun.* **9**, 4037 (2018).
19. Kato, Y. et al. High-power all-solid-state batteries using sulfide superionic conductors. *Nat. Energy* **1**, 16030 (2016).
20. Ye, L. et al. Toward higher voltage solid-state batteries by metastability and kinetic stability design. *Adv. Energy Mater.* **10**, 2001569 (2020).
21. Fitzhugh, W., Wu, F., Ye, L., Su, H. & Li, X. Strain-stabilized ceramic-sulfide electrolytes. *Small* **15**, 1901470 (2019).
22. Saroha, R., Panwar, A. K., Sharma, Y., Tyagi, P. K. & Ghosh, S. Development of surface functionalized ZnO-doped $LiFePO_4$/C composites as alternative cathode material for lithium ion batteries. *Appl. Surf. Sci.* **394**, 25–36 (2017).
23. Jin, S. et al. Covalently connected carbon nanostructures for current collectors in both the cathode and anode of Li–S Batteries. *Adv. Mater.* **28**, 9094–9102 (2016).
24. Kang, B. & Ceder, G. Battery materials for ultrafast charging and discharging. *Nature* **458**, 190–193 (2009).
25. Wang, S. et al. Lithium chlorides and bromides as promising solid-state chemistries for fast ion conductors with good electrochemical stability. *Angew. Chem. Int. Ed.* **58**, 8039–8043 (2019).
26. Fitzhugh, W., Ye, L. & Li, X. The effects of mechanical constriction on the operation of sulfide based solid-state batteries. *J. Mater. Chem. A* **7**, 23604–23627 (2019).
27. Schwietert, T. K. et al. Clarifying the relationship between redox activity and electrochemical stability in solid electrolytes. *Nat. Mater.* **19**, 428–435 (2020).

Methods

$Li_{5.5}PS_{4.5}Cl_{1.5}$ (LPSCl) was prepared by high energy ball milling, followed by a post annealing treatment. Stoichiometric amounts of powders of Li_2S (>99.9% purity, Alfa Aesar), P_2S_5 (>99% purity, Sigma Aldrich) and LiCl (>99% purity, Alfa Aesar) were milled for 16 h in a planetary mill PM200 (Retsch GmbH, Germany) under a protective Argon atmosphere followed by sintering at 550 °C in a quartz tube.

$Li_{9.54}Si_{1.74}(P_{0.9}Sb_{0.1})_{1.44}S_{11.7}Cl_{0.3}$ (LSPS) were prepared using the same method. Li_2S (>99.9% purity, Alfa Aesar), SiS_2 (>99% purity, American Elements), P_2S_5 (>99% purity, Sigma Aldrich), Sb_2S_5 (Sigma Aldrich) and LiCl (>99% purity, Alfa Aesar) were ball milled for 40 h (LSPS) followed by sintering[18]. All heating treatments were under Ar gas flow protection.

The 0.63-cm-diameter Li foil with the thickness of 25 µm (Lithium Innovations LLC) was covered by a 0.95-cm-diameter graphite film with a weight ratio of graphite (BTR, China) and PTFE as 95:5. The capacity ratio of Li and graphite is from 2.5:1 to 10:1. The cathode layer was made by mixing 3 wt% PTFE, 29.1 wt% solid electrolyte and 67.9 wt% $LiCoO_2$ (Sigma Aldrich) or single-crystal $LiNi_{0.8}Mn_{0.1}Co_{0.1}O_2$ of 2–4-µm particle size (tapping density ~2 g cm^{-3}, XTC, China) with a loading of ~2 mg cm^{-2}. 140 mg $Li_{10}Ge_1P_2S_{12}$ (ref. [21]), LSPS or LPSCl was employed as electrolytes. For the multilayer design, 40 mg LPSCl and 100 mg LGPS (or LSPS) were used. The anode-solid electrolyte-cathode for half-battery or anode-solid electrolyte-anode for symmetric battery were pressed together in a homemade pressurized cell at 467 MPa and kept at 50–250 MPa during testing. The symmetric battery has the structure of Li–graphite–solid electrolyte–graphite–Li and the non-symmetric cell is Li–graphite–LPSCl–LGPS–LPSCl–NMC for Fig. 3 and Li–graphite–LPSCl, or Li–graphite–LPSCl–LGPS, or Li–graphite–LPSCl–LGPS–LPSCl for Extended Data Fig. 2. The density of the multilayer after the initial cold press is measured as 1.8 g cm^{-3}, equivalent to 93% theoretical density of the sulfide layers (that is, around 7% porosity). Such porosity can be eliminated with a minimum operating stack pressure near 30 MPa as shown in our previous work[20]. All batteries were assembled in an argon atmosphere glovebox and the galvanostatic battery cycling test was performed on an ArbinBT2000 workstation. The humidity of the battery testing environment was controlled inside a Memmert hpp110.

The liquid cells were assembled using Li metal as the anode, glass fibre as the separator and 1 M $LiPF_6$ in EC/DMC (v:v = 1:1) as the electrolyte. A cathode film with the same active material loading of 2 mg cm^{-2} was applied, with the ratio of NMC811:Carbon:PTFE = 85:10:5. The batteries were assembled in a Swagelok cell and cycled at room temperature with a cut-off voltage of 2–4.3 V. Optical images were taken from the camera embedded in the Thermo Scientific K-Alpha$^+$ or an optical microscope in the glovebox, and XPS data were obtained from the same tool with a beam size of 70 µm or 400 µm. Cross-sectional SEM imaging of the pellet was performed on a Supra 55 SEM with an acceleration of 5 keV. SEM samples were prepared following the same procedure, including the uncycled one. They were then sealed inside a plastic bag in the glovebox before transferring to SEM, where the bag was opened for a quick loading of sample into the SEM chamber to minimize air contamination. XRD data were collected on a Rigaku Miniflex. Measurements were taken within a 2θ range from 15° to 80°, with a 0.02° step and a scan speed of 0.24 s per step. The sample was sealed by a Kapton film in the glovebox before transferring to the XRD. Battery cycling data and materials characterizations were repeated multiple times with good reproducibility.

Data availability

The data that support the findings of this study are available from the corresponding author upon reasonable request.

Acknowledgements The work was supported by the Dean's Competitive Fund for Promising Scholarship at Harvard University and the Harvard Data Science Initiative Competitive Research Fund. The SEM and XPS experiments were conducted at the Center for Nanoscale Systems (CNS) at Harvard University, supported by the National Science Foundation.

Author contributions X.L. and L.Y. conceived the multilayer design. X.L. supervised all aspects of the research. L.Y. performed the experiments. L.Y. and X.L. analysed the results and wrote the manuscript.

Competing interests X.L. and L.Y. report a US provisional patent application of Batteries with Solid State Electrolyte Multilayers filed on 30 October 2020. Application serial no. 63/108,075.

Additional information
Supplementary information The online version contains supplementary material available at https://doi.org/10.1038/s41586-021-03486-3.
Correspondence and requests for materials should be addressed to X.L.
Peer review information *Nature* thanks the anonymous reviewer(s) for their contribution to the peer review of this work. Peer reviewer reports are available.
Reprints and permissions information is available at http://www.nature.com/reprints.

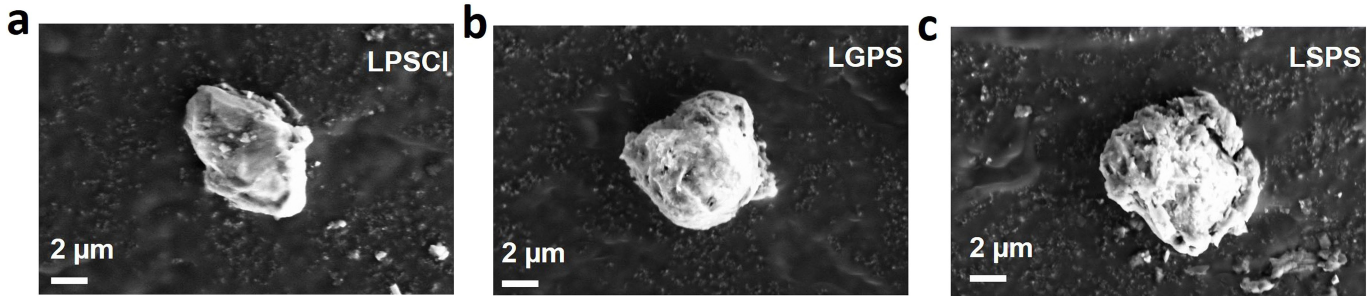

Extended Data Fig. 1 | SEM images of LPSCl, LGPS and LSPS particles. a–**c**, SEM images of LPSCl (**a**), LGPS (**b**) and LSPS (**c**) particles.

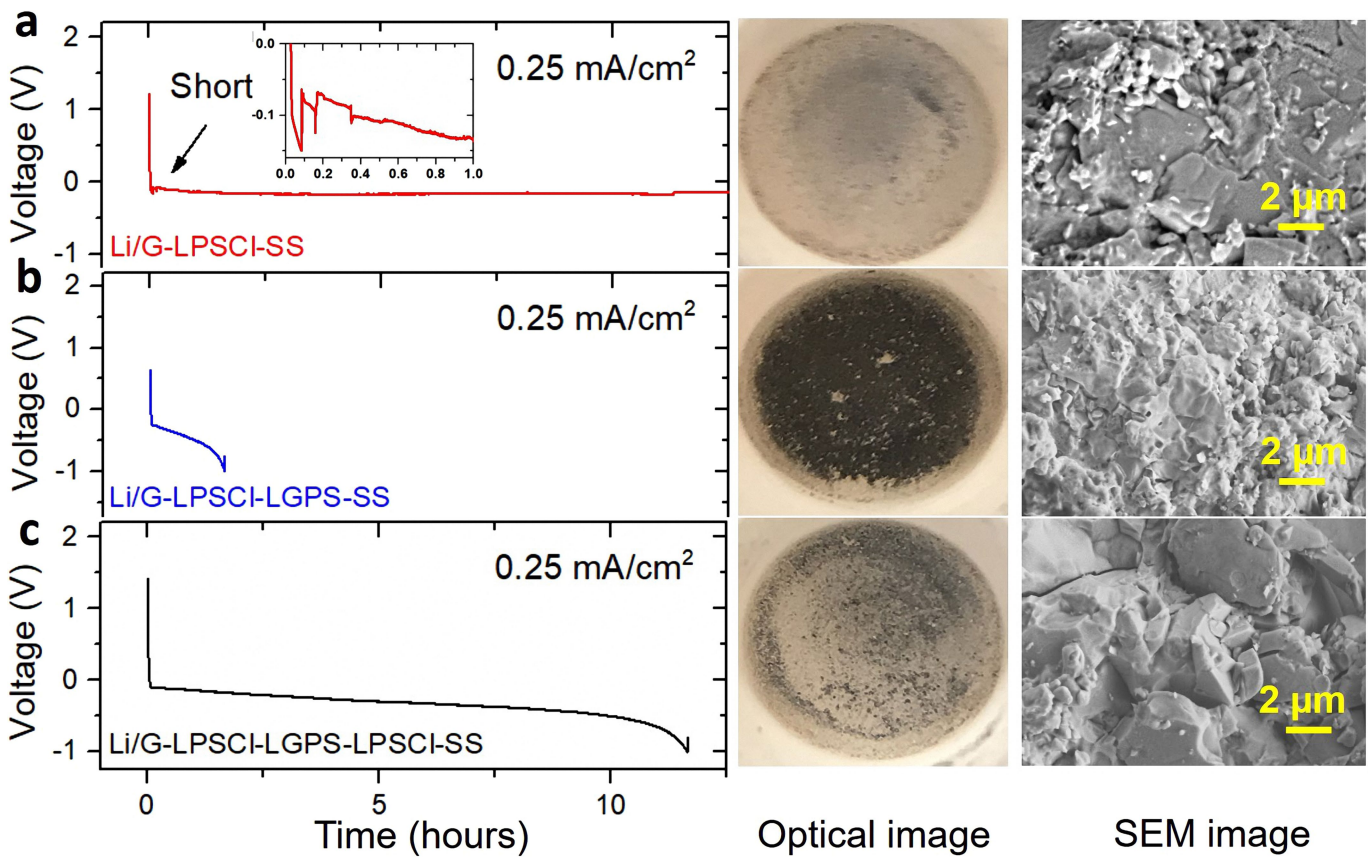

Extended Data Fig. 2 | Electrochemical voltage profiles, optical and SEM images of lithium discharged asymmetric batteries with different electrolytes. Asymmetric batteries with Li/G as anode (lithium capacity loading = 3 mAh cm^{-2}), stainless steel (SS) current collector as cathode, and solid electrolytes as separator were assembled. Lithium was enforced to deposit on the surface of solid electrolytes at 0.25 mA cm^{-2}. Different electrochemical behaviours and surface information were observed. **a**, Short-circuiting happened immediately after lithium was deposited on the surface of pure LPSCl pellet. A metallic colour (silver or grey) was observed from the optical image and a small level of cracking was observed from the SEM image. **b**, Voltage ramping up quickly after lithium was deposited on the surface of pure LGPS pellet in a few hours. Decomposition (dark black) was observed from the optical image and no crack was observed from the SEM image. **c**, Voltage ramping up gradually, reaching cut-off voltage after lithium was fully deposited on the surface of the LGPS separated LPSCl pellet. Metallic colour (silver or grey) on large area was observed from the optical image and cracks were observed from the SEM image.

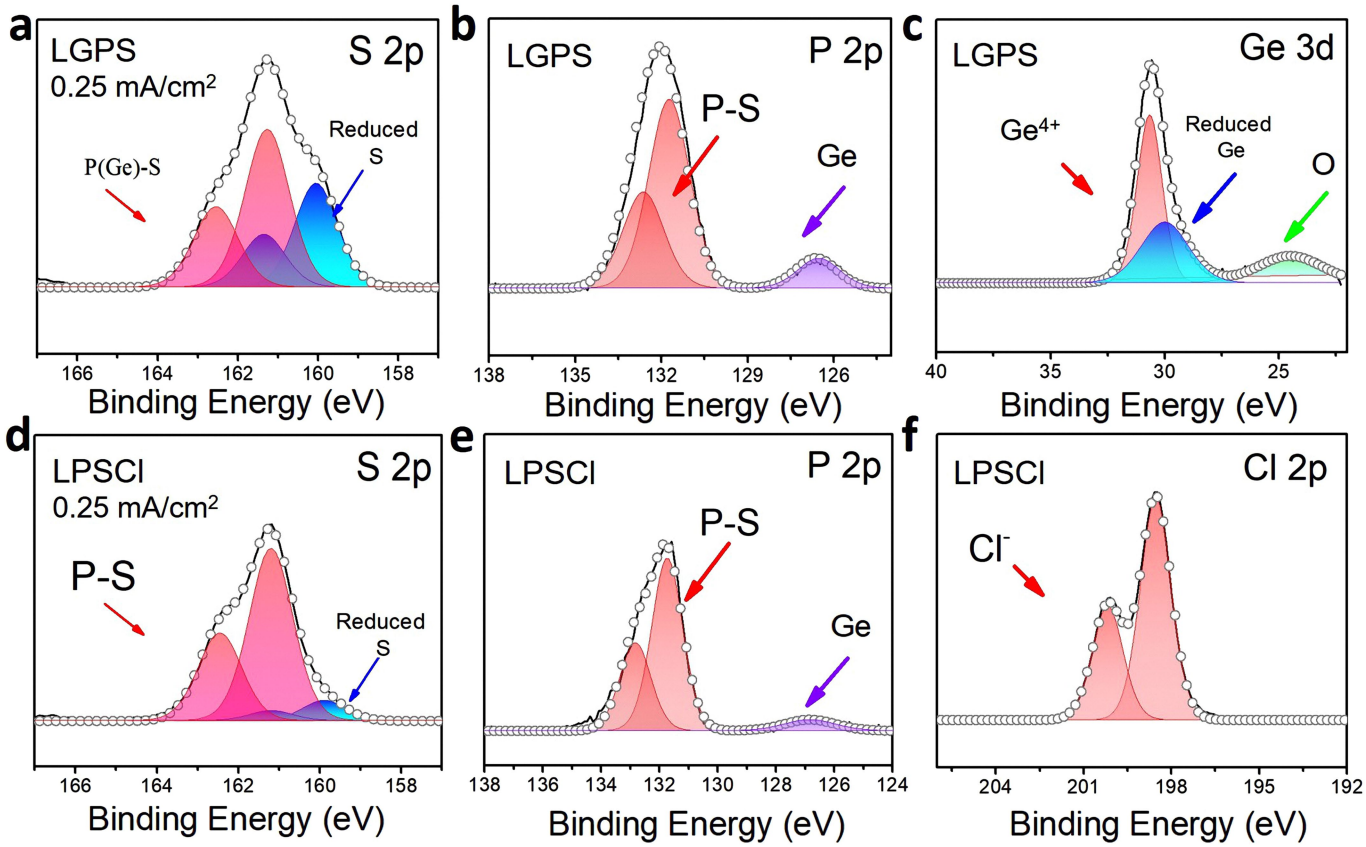

Extended Data Fig. 3 | XPS characterization on the dark region of LGPS and LPSCl after lithium discharge. a–c, XPS data of the black region on the LGPS surface after lithium discharging at 0.25 mA cm^{-2} (shown in Supplementary Fig. 2b) with the chemical information of S (**a**), P (**b**) and Ge (**c**). **d–f**, XPS data of the silver region on the LPSCl surface after lithium discharging (shown in Supplementary Fig. 2c) with the chemical information of S (**d**), P (**e**) and Cl (**f**). The beam size of XPS is 400 μm.

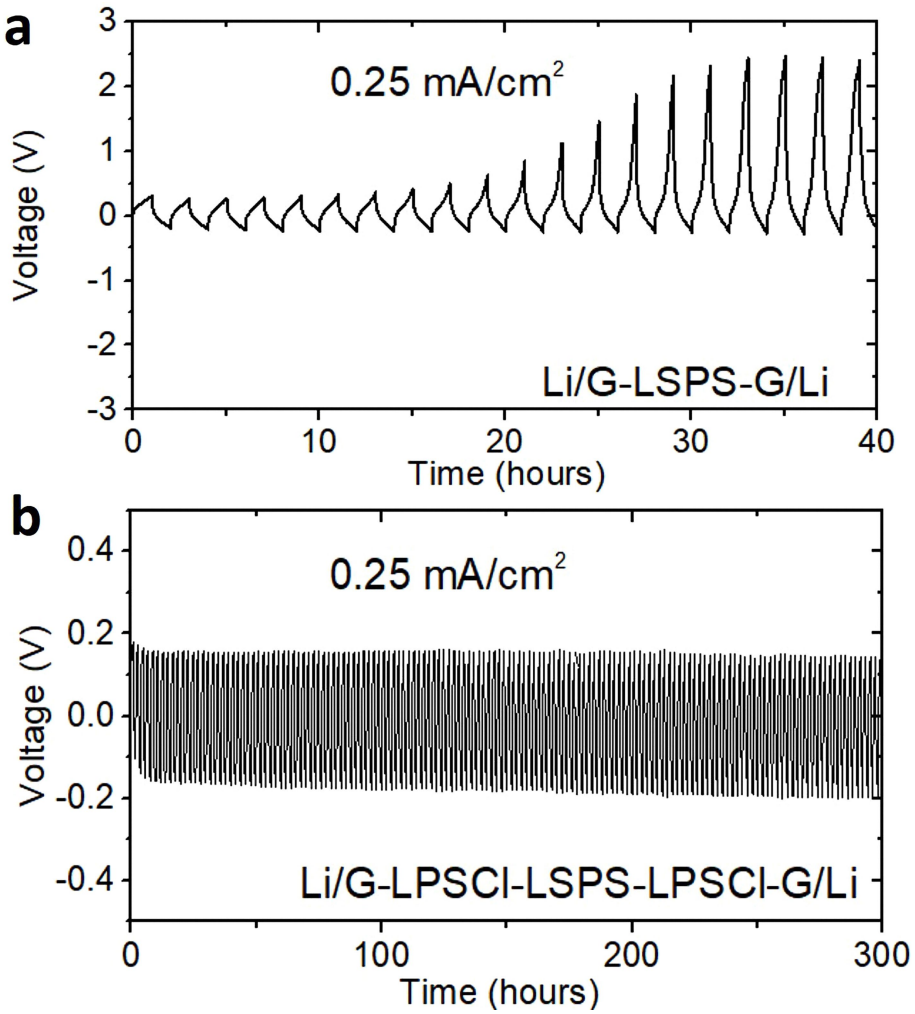

Extended Data Fig. 4 | Performance difference of LSPS as the single layer and the central layer of multilayer in symmetric battery configurations. **a**, Symmetric battery with $Li_{9.54}Si_{1.74}(P_{0.9}Sb_{0.1})_{1.44}S_{11.7}Cl_{0.3}$ (LSPS) as electrolyte and graphite covered lithium (Li/G) as electrodes. **b**, Symmetric battery with the combination of $Li_{9.54}Si_{1.74}(P_{0.9}Sb_{0.1})_{1.44}S_{11.7}Cl_{0.3}$ (LSPS) and $Li_{5.5}PS_{4.5}Cl_{1.5}$ (LPSCl) in the configuration of LPSCl–LSPS–LPSCl as electrolyte and graphite covered lithium as electrodes.

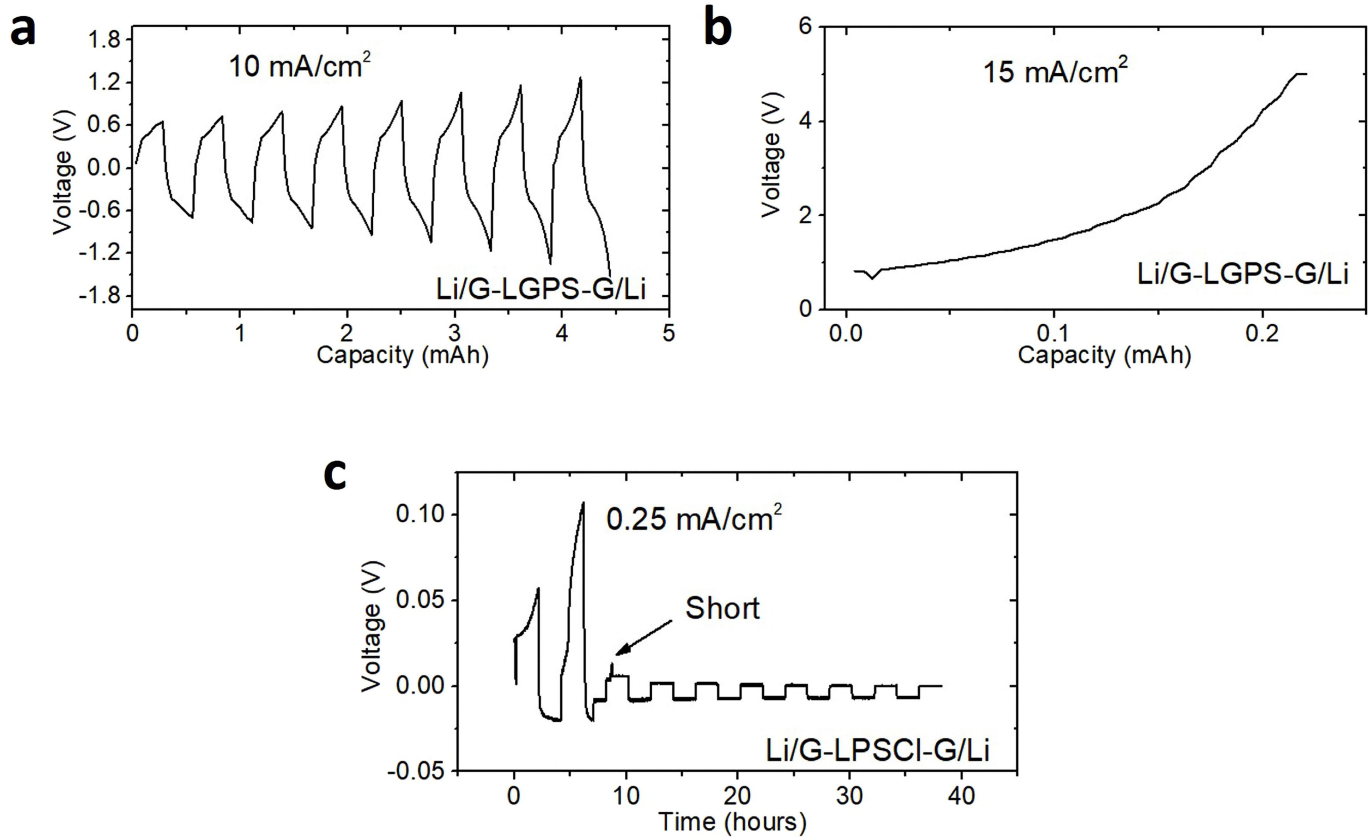

Extended Data Fig. 5 | Cycling performance of symmetric batteries with LGPS or LPSCl as the single solid electrolyte layer. a, High rate (10 mA cm^{-2}) cycling for $Li_{10}Ge_1P_2S_{12}$ (LGPS) symmetric battery with Li/G as electrodes. The over potential starts from 0.6 V and quickly ramp up to over 1.5 V in the first few cycles. **b**, High rate (15 mA cm^{-2}) cycling for LGPS symmetric battery with Li/G as electrodes. The over potential ramping up to over 5 V in the first cycle. **c**, Symmetric battery with LPSCl as electrolyte and Li/G as electrodes, cycling at 0.25 mA cm^{-2}. Short-circuiting shows up in the first two cycles.

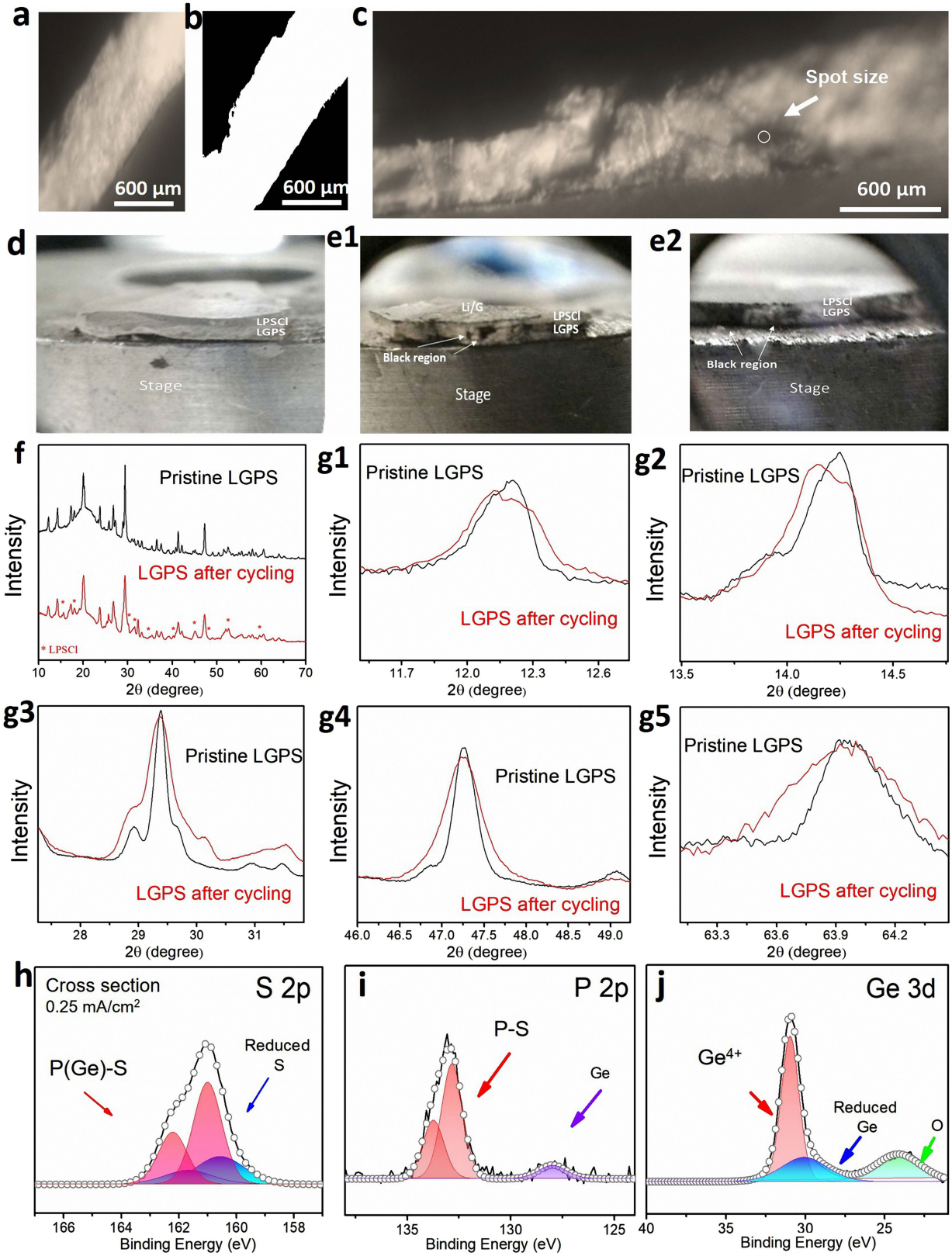

Extended Data Fig. 6 | See next page for caption.

Extended Data Fig. 6 | Optical image, XRD and XPS of cross-sections of symmetric batteries before and after cycling. a, Optical image of cross-section of Li/G-LPSCl-LGPS-LPSCl-G/Li after 300 h cycling at 0.25 mA cm^{-2} at room temperature, showing another region without decomposition. **b**, Post-treated image of **a** in only black and white. **c**, Optical image of cross-section of Li/G–LPSCl–LGPS–LPSCl–G/Li after 30 cycles at 20 mA cm^{-2} at 55 °C. XPS spot size is marked in the black region for a comparison with the size of the black region. **d**, Optical image of the cross-section of the LPSCl–LGPS–LPSCl pellet before cycling. **e**, Optical image of the cross-section of the LPSCl–LGPS–LPSCl pellet after 300 h cycling at 0.25 mA cm^{-2} (**e1**) and 30 cycles at 20 mA cm^{-2} (**e2**). The images in **d** and **e** are from the same pellet in **a** and **c** in a larger view, which were taken by an optical microscope in the glovebox. **f**, XRD of LGPS before and after cycling at 0.25 mA cm^{-2} for 300 h, with features of XRD peaks shown in **g1**–**g5**. **h**–**j**, XPS measurement of S 2*p* (**h**), P 2*p* (**i**) and Ge 3*d* (**j**) on the black region in the cross-section of the sandwich pellet after battery cycling at 0.25 mA cm^{-2} for 300 h. The beam size of the XPS is 70 μm.

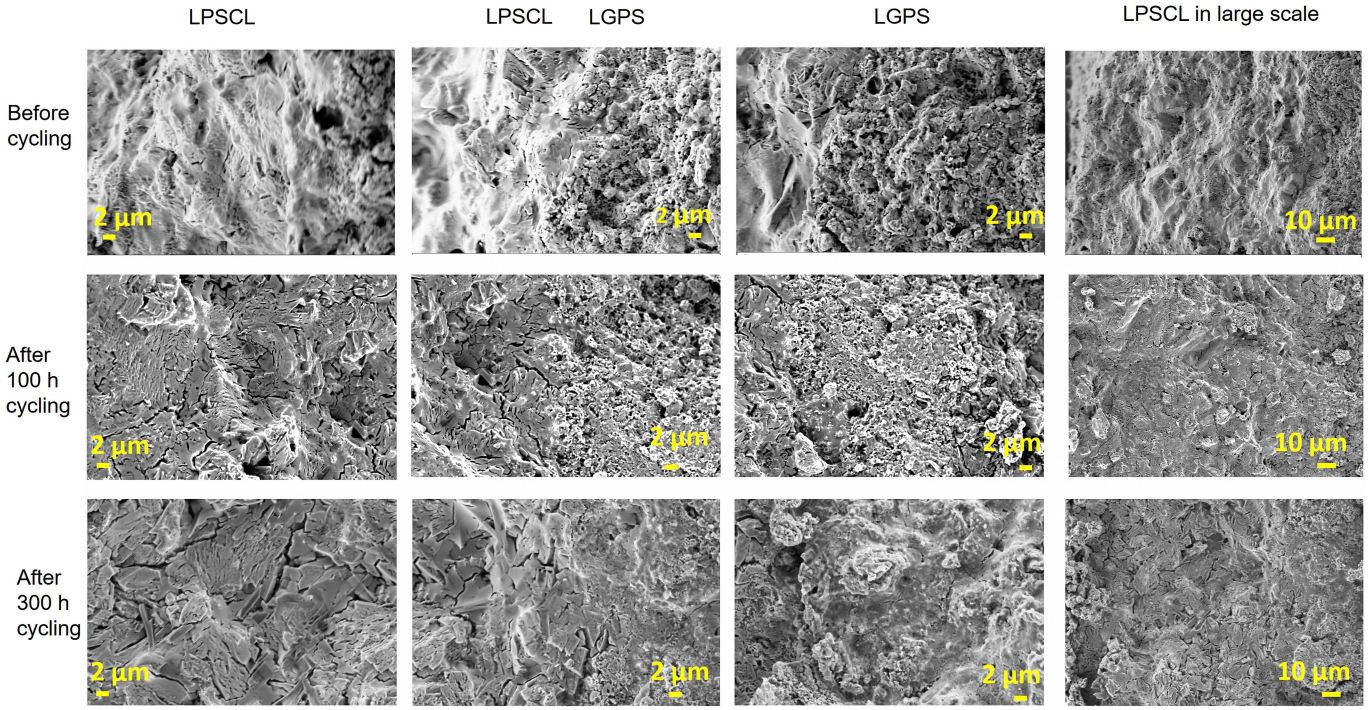

Extended Data Fig. 7 | Morphology difference of LGPS and LPSCl before and after cycling. SEM images of the solid electrolytes before cycling (first row), and after cycling for 100 h (second row) and 300 h (third row) in the region of LPSCl, LGPS, and their transition areas. The fourth column: LPSCl side with a 10-µm scale bar. The SEM images were from the symmetric battery in the configuration of Li/G–LPSCl–LGPS–LPSCl–G/Li.

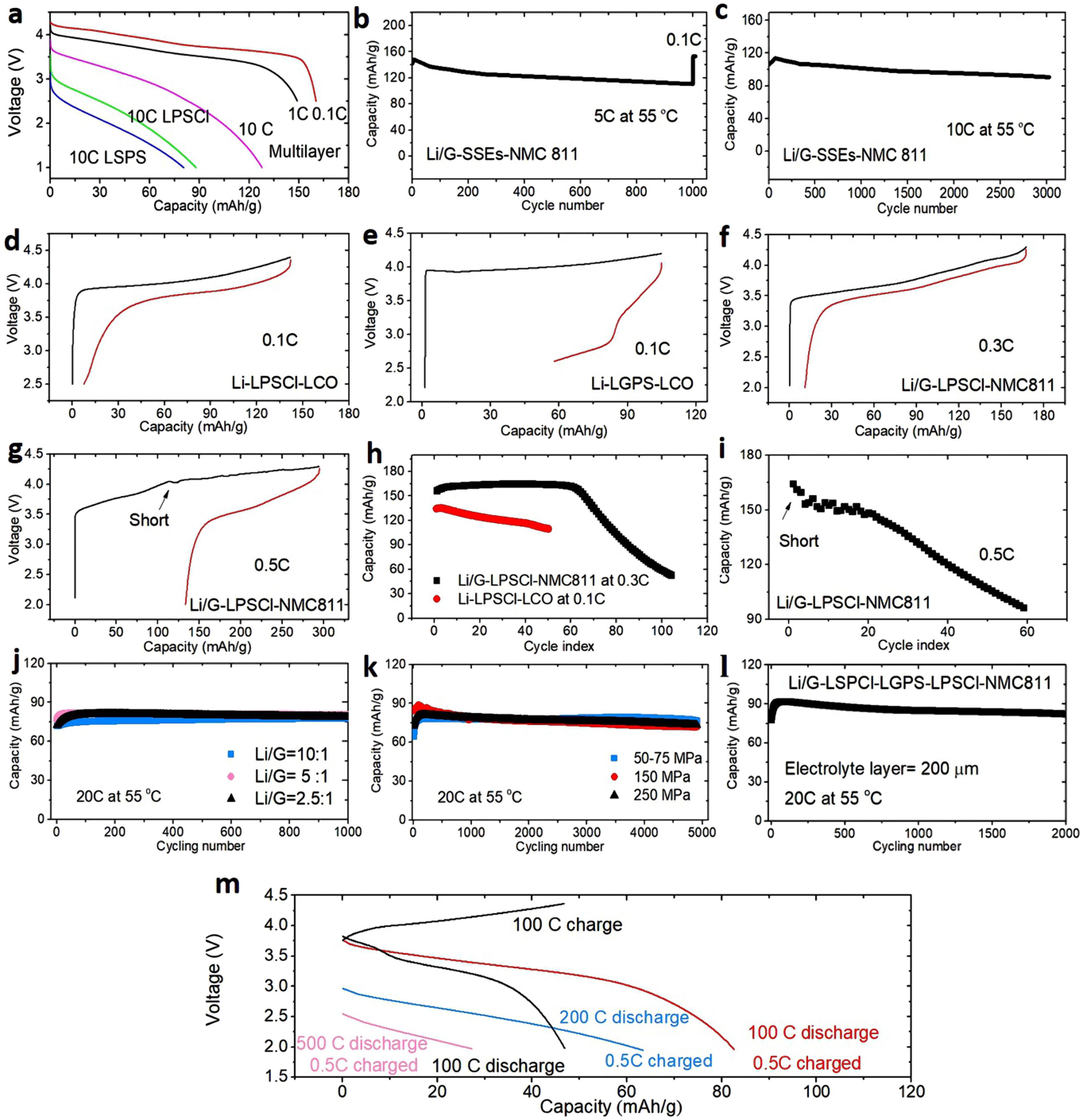

Extended Data Fig. 8 | Half-battery cycling performance using pure LGPS and/or LPSCl as electrolytes. a, The discharging profiles of graphite covered Li paired with $LiNi_{0.8}Mn_{0.1}Co_{0.1}O_2$ (Li/G-NMC811) batteries, using $Li_{5.5}PS_{4.5}Cl_{1.5}$ (LPSCl, green 10C), $Li_{9.54}Si_{1.74}(P_{0.9}Sb_{0.1})_{1.44}S_{11.7}Cl_{0.3}$ (LSPS, blue 10C), and multilayer LPSCl-LSPS-LPSCl configuration (purple 10C, black 1C, red 0.1C) as the electrolyte. The batteries were first charged at 0.1C and then discharged at various rates at room temperature. **b**, **c**, The cycling performance of the same multilayer battery at 5C (**b**) and 10C (**c**) in the range of 2.5–4.3 V in the environment without humidity control (55 °C). **d**, **e**, The first charge and discharge profiles of Li-$LiCoO_2$ (Li-LCO) batteries with (**d**) $Li_{5.5}PS_{4.5}Cl_{1.5}$ (LPSCl) and (**e**) $Li_{10}Ge_1P_2S_{12}$ (LGPS) as the electrolyte. Uncoated LCO and $LiNbO_3$-coated LCO is applied for LPSCl and LGPS, respectively. **f**, **g**, The first charge and discharge profiles of graphite covered Li paired with $LiNi_{0.8}Mn_{0.1}Co_{0.1}O_2$ (Li/G-NMC811) batteries with LPSCl as the electrolyte at (**f**) 0.3C and (**g**) 0.5C; along with the cycling performance at (**h**) 0.3C (LCO at 0.1C is also shown) and (**i**) 0.5C. All batteries in **d**–**i** were tested at room temperature. The battery configuration and materials used are summarized in Supplementary Table 2. **j**, Cycling performance of solid-state battery with multilayer electrolytes at different Li/graphite capacity ratios of 10:1, 5:1 and 2.5:1. **k**, Cycling performance of solid-state battery with multilayer electrolytes under different operating pressures of 50–75 MPa, 150 MPa and 250 MPa. **l**, Cycling performance of solid-state battery with thin multilayer: Li/G–LPSCl (100 μm)–LSPS (50 μm)–LPSCl (50 μm)–NMC811. **m**, High-power voltage profile of the Li/G–LPSCl–LSPS–LPSCl–NMC811 battery at 100C–500C at 55 °C with a cut-off voltage of 2–4.3 V. Red, blue and pink curves are from batteries first charged at 0.5C and then discharged at high C rates, and black curves are at 100C charge and discharge. 1C = 0.43 mA cm^{-2}.

Extended Data Table 1 | Mechanical and (electro)chemical properties of different electrolytes

	Ionic conductivity (mS/cm)[a]	Electronic conductivity (mS/cm)[b]	Particle size[c]	Young's modulus[d] (GPa)
$Li_{10}Ge_1P_2S_{12}$ (LGPS)	5.1	$7.4*10^{-5}$	1-3 μm	37.2
$Li_{5.5}PS_{4.5}Cl_{1.5}$ (LPSCl)	6.2	$2.8*10^{-5}$	1-3 μm	22–30
$Li_{9.54}Si_{1.74}(P_{0.9}Sb_{0.1})_{1.44}S_{11.7}Cl_{0.3}$ (LSPS)	8.8	$1.2*10^{-5}$	1-3 μm	20-30

Properties including electronic and ionic conductivities, particle size, and Young's modulus of different electrolytes.

[a]All measurements are based on cold press without heating treatment.

[b]The orders of magnitude of electronic conductivity measured in the work are consistent with the literature

[c]Particle size is measured from SEM images

[d]Modulus values are from previous studies[12,13,17,18]

Extended Data Table 2 | Battery configurations and materials ratios applied in this work

	Anode	Electrolyte	Cathode
Li-LGPS-LCO	lithium	140 mg LGPS	70wt% $LiNbO_3$ coated LCO 30wt% LGPS 3wt% extra PTFE
Li-LPSCl-LCO	lithium	140 mg LPSCl	70wt% uncoated LCO 30wt% LPSCl 3wt% extra PTFE
Li/G-LPSCl-NMC811	graphite covered lithium (capacity ratio G:Li = 1:2.5)	140 mg LPSCl	70wt% NMC811 30wt% LPSCl 3wt% extra PTFE
Li/G-LPSCl-LSPS-LPSCl-NMC811	graphite covered lithium (capacity ratio G:Li = 1:2.5)	20 mg LPSCl 100 mg LSPS 20 mg LPSCl	70wt% NMC811 30wt% LPSCl 3wt% extra PTFE
Li/G-LSPS-LPSCl-NMC811	graphite covered lithium (capacity ratio G:Li = 1:2.5)	120 mg LSPS 20 mg LPSCl	70wt% NMC811 30wt% LPSCl 3wt% extra PTFE